UDC 532

COMPUTATIONAL MODELING OF A PASSIVE-PITCH LOW-WIND VERTICAL-AXIS WIND TURBINE

*Muzaffarov S.A., Maratov Kh.U., Hamdamov M.M.
*sardorbekmuzaffarov50@gmail.com
Institute of mechanics and seismic stability of structures named after M.T. Urazbaev, 33, str. Durman yuli, Tashkent, 100125 Uzbekistan.

This paper presents a three-dimensional numerical study of a novel vertical-axis wind turbine (VAWT) with a unique aerodynamic profile and a passive blade-pitch mechanism. Rectangular blades are mounted on horizontal axes through articulated bearings and rotate freely up to 90°, constrained by a pin-and-belt system: on the power stroke the blades hit a stopper to capture maximum energy, while on the return stroke they open to reduce drag, enabling efficient operation at low wind speeds (3–5 m/s) with stable torque. After a grid-independence study, the aerodynamics were analyzed in COMSOL Multiphysics by solving the RANS equations. Four turbulence models (SST, $k-\varepsilon$, $k-\omega$, RNG) were compared; the SST model best captured flow separation and wake structures. Power-coefficient (C_p) versus tip-speed-ratio (TSR) curves were obtained and validated against laboratory data (relative error $< 5\%$).

Keywords: Navier–Stokes equations, wind turbine, Comsol Multiphysics, computational fluid dynamics, renewable energy, velocity, pressure.

Citation: Muzaffarov S.A., Maratov Kh.U., Hamdamov M.M. 2026. Computational modeling of a passive-pitch low-wind vertical-axis wind turbine. *Problems of Computational and Applied Mathematics.* 3(73): 61-74.

DOI: https://doi.org/10.71310/pcam.3_73.2026.05

1 Introduction

Wind energy is vital for sustainable power, but optimizing aerodynamic performance at low wind speeds (3–5 m/s) remains a technical challenge. While vertical-axis wind turbines (VAWTs) are well-suited for such environments due to their omnidirectional operation and low noise, conventional designs struggle with early flow separation and poor self-starting capabilities at low Reynolds numbers.

Extensive literature addresses VAWT optimization. Studies highlight the importance of airfoil geometry and inertia for self-starting [1, 3], as well as stability under pulsating winds [2]. Advances in turbulent flow modeling [4, 5] and turbine placement [6] have improved overall efficiency. Despite certain computational fluid dynamics (CFD) limitations [7], recent research heavily focuses on active and passive flow-control techniques [8–10] to mitigate boundary-layer separation on turbine blades.

Recent CFD studies have evaluated various blade profiles, including NASA and Savonius types [11–13], often employing RANS models to analyze complex flows [14–18]. However, most focus on wind speeds exceeding 7 m/s. While specialized designs like the Archimedes screw [18] address low flows, a research gap exists regarding 3D aerodynamics of non-conventional VAWTs optimized for stable generation at speeds as low as 3 m/s. Passive flow control, such as surface roughness [22], has proven effective in mitigating low-speed flow instabilities (e.g., expanding compressor operating range and stall mar-gin), highlighting the potential of passive mechanisms.Unlike traditional fixed-design VAWTs, the proposed system features self-adjusting hinged rectangular blades.

This novel mechanism switches between a closed (high-drag) energy-extraction position and an open (low-resistance) return position. Offsetting the blades from the center axis minimizes turbulent interference and improves tangential velocity, boosting efficiency in low-Reynolds-number urban conditions.To bridge the existing research gap, this study presents a 3D numerical investigation of this novel VAWT. Optimized for high torque at low velocities, its aerodynamic profile and mechanical operation fundamentally differ from conventional drag-based models. Using COMSOL Multiphysics to solve the RANS equations, a comparative analysis of SST, $k-\varepsilon$, $k-\omega$ and RNG turbulence models is conducted to determine the most accurate predictor of boundary layer separation—a critical phenomenon in low-wind conditions.

2 Materials and Methods

The Developing high-efficiency vertical-axis wind turbines (VAWTs) capable of operating in low-wind regimes is a crucial task for sustainable energy. The subject of this study is a novel, patented VAWT that features a fundamentally different aerodynamic approach compared to conventional Savonius or Darrieus designs.

The core innovation of this device lies in its passive blade-pitch control mechanism. Rectangular blades, mounted on horizontal axes via articulated bearings, possess restricted freedom of movement. This configuration is specifically engineered to maximize the drag coefficient during the power stroke and minimize it during the return stroke.

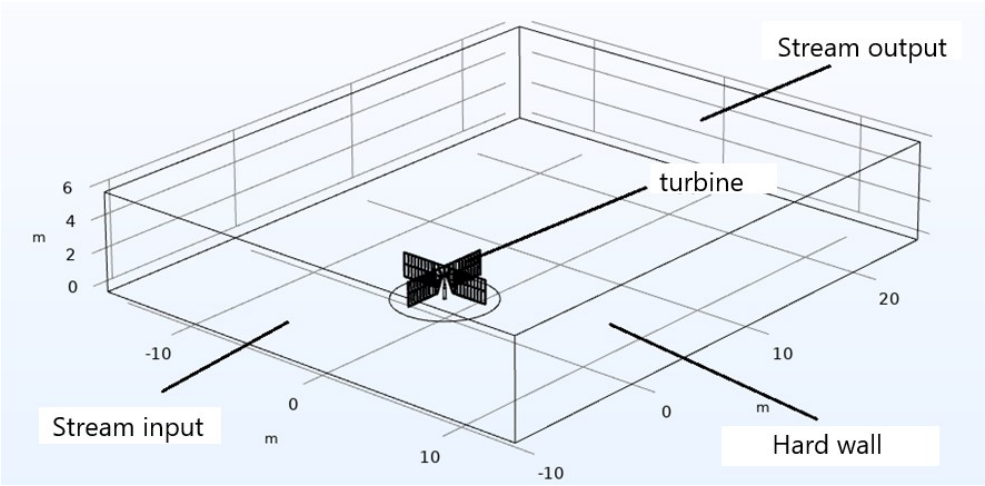

Figure 1 View of the wind generator inside the computational domain

Numerical simulation was performed within a 3D computational domain (20 m width $\times$ 30 m length $\times$ 6 m height) to accurately capture aerodynamic interactions. A Cartesian coordinate system (X, Y, Z) was defined with its origin $(0, 0, 0)$ at the turbine stand base. The OX-axis aligns with the primary wind direction (inlet to outlet), while the OZ-axis extends vertically upward. The VAWT blades ($L = 3$ m) are elevated 0.5 m above the ground to account for near-ground boundary layer effects. To eliminate blockage effects and ensure domain-size independence, boundaries were placed sufficiently far from the rotor. The chosen domain volume optimizes computational economy and flow-field accuracy, capturing pressure gradients and downstream wake development without wall interference. The geometry for problem formulation and mesh generation strictly adheres to the parameters in Fig. 2, ensuring consistency between the physical prototype and the numerical model.

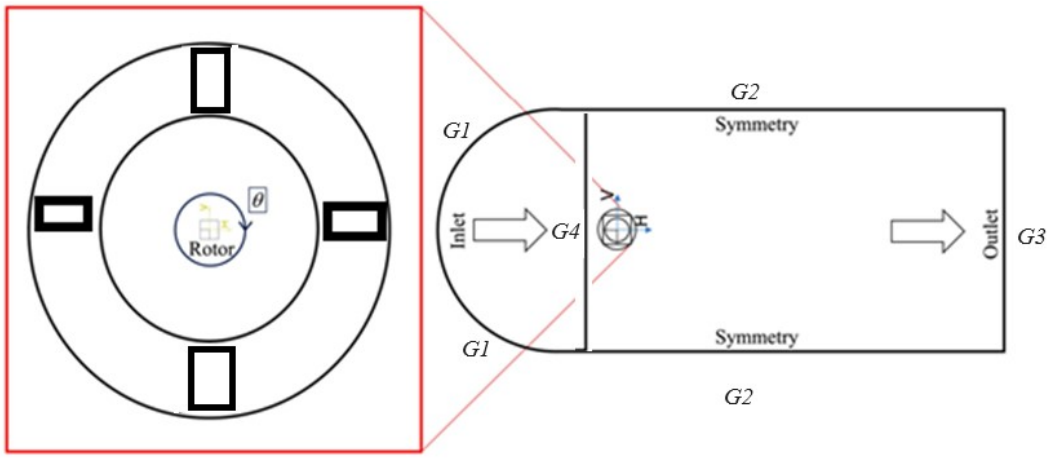

Figure 2 Profile geometry

To reduce computational volume by excluding undisturbed flow zones, a semi-circular inlet boundary ($(x^2 + y^2 = R^2 = 15^2\text{m}) \cap x \leqslant 0$) is defined to set incoming wind parameters (velocity, pressure, kinetic energy). Zero-flux (slip) conditions are applied at the lateral boundaries ($x \geqslant 0, \cap\, y = \pm L_y$), while an outflow condition is implemented at the domain exit ($X = 2.5\text{m}$, $y \leqslant 15\text{m}$). The 3D transient flow is modeled as incompressible and isothermal, justified by the low Mach number ($M < 0.3$) at operational wind speeds of 3–5 m/s. To ensure strict mass and momentum conservation near the solid boundaries of the rotating blades, the conservative Reynolds-Averaged Navier-Stokes (RANS) equations are employed [23]. The governing equations are closed using a velocity inlet, an atmospheric-pressure outlet, and no-slip conditions on the moving rotor surfaces.

To model a three-dimensional turbulent air flow, the equation of the law of conservation of mass was used [21]:

$$\frac{\partial \rho}{\partial t} + \frac{\partial(\rho u)}{\partial x} + \frac{\partial(\rho v)}{\partial y} + \frac{\partial(\rho w)}{\partial z} = 0$$

and the Reynolds-averaged momentum conservation equations:

$$\frac{\partial(\rho u)}{\partial t} + \operatorname{div}(\rho u \mathbf{u}) = -\frac{\partial p}{\partial x} + \operatorname{div}(\mu \operatorname{grad} u) +$$
$$+ \left[-\frac{\partial\left(\rho\overline{u'u'}\right)}{\partial x} - \frac{\partial\left(\rho\overline{u'v'}\right)}{\partial y} - \frac{\partial\left(\rho\overline{u'w'}\right)}{\partial z} \right] + S_{Mx},$$
$$\frac{\partial(\rho v)}{\partial t} + \operatorname{div}(\rho v \mathbf{u}) = -\frac{\partial p}{\partial y} + \operatorname{div}(\mu \operatorname{grad} v) +$$
$$+ \left[-\frac{\partial\left(\rho\overline{u'v'}\right)}{\partial x} - \frac{\partial\left(\rho\overline{v'v'}\right)}{\partial y} - \frac{\partial\left(\rho\overline{v'w'}\right)}{\partial z} \right] + S_{My},$$
$$\frac{\partial(\rho w)}{\partial t} + \operatorname{div}(\rho w \mathbf{u}) = -\frac{\partial p}{\partial z} + \operatorname{div}(\mu \operatorname{grad} w) +$$
$$+ \left[-\frac{\partial\left(\rho\overline{u'w'}\right)}{\partial x} - \frac{\partial\left(\rho\overline{v'w'}\right)}{\partial y} - \frac{\partial\left(\rho\overline{w'w'}\right)}{\partial z} \right] + S_{Mz}.$$

Here u, v, w, u', v', w' — average and pulsation components of the velocity vector; p — average pressure; μ, μ_t — laminar and turbulent coefficients of dynamic viscosity; $S_{Mx} = = S_{My} = 0, S_{Mz} = -\rho g$ — components of the Archimedes force.

To accurately predict the novel VAWT's aerodynamic behavior, selecting an appropriate turbulence model is critical. While methods like Large Eddy Simulation (LES) and Direct Numerical Simulation (DNS) offer high fidelity, their extreme computational demands make RANS-based models more practical for iterative design optimization [15, 16]. Among RANS approaches, the SST (Shear Stress Transport) k-ω model was selected as the primary numerical tool. The standard k-ω model often under predicts flow separation near solid walls [18–20], while the standard k-ω model is overly sensitive to free-stream turbulence. The SST formulation effectively bridges this gap by employing k-ω in the viscous sublayer to capture early separation and dynamic stall under severe adverse pressure gradients (typical at 3–5 m/s), seamlessly transitioning to k-ω in the far-field [19]. Accurately capturing these near-wall boundary layer physics and tangential velocity gradients is essential for calculating torque and the power coefficient (C_p) in low-wind urban regimes. To support this, numerical solutions were obtained using high-order discretization schemes, preventing numerical diffusion and ensuring high-quality aerodynamic analysis [12–14].

$$\frac{\partial}{\partial x_i}(\rho k u_i) = \frac{\partial}{\partial x_j}\left[\left(\mu + \frac{\mu_t}{\sigma_k}\right)\frac{\partial k}{\partial x_j}\right] + G_k + G_b - \rho\varepsilon - Y_M + S_k,$$

$$\frac{\partial}{\partial x_i}(\rho \varepsilon u_i) = \frac{\partial}{\partial x_j}\left[\left(\mu + \frac{\mu_t}{\sigma_\varepsilon}\right)\frac{\partial \varepsilon}{\partial x_j}\right] + C_{1\varepsilon}\frac{\varepsilon}{k}(G_k + C_{3\varepsilon}G_b) - C_{2\varepsilon}\rho\frac{\varepsilon^2}{k} + S_\varepsilon.$$

Turbulent viscosity is determined by the formula:

$$\mu_t = \rho C_\mu \frac{k^2}{\varepsilon}.$$

While the standard $k{-}\varepsilon$ model is computationally efficient and robust for fully turbulent flows, its assumption of isotropic eddy viscosity limits its accuracy in predicting complex phenomena such as high-strain rates, large-scale eddy development, and curvature-induced turbulence. To address these limitations, the RNG (Re-Normalization Group) $k{-}\varepsilon$ model was employed. Derived via rigorous statistical techniques, the RNG variant offers key analytical enhancements over the standard model. It solves the following transport equations for turbulent kinetic energy (k) and its dissipation rate (ε):

$$\frac{\partial k}{\partial t} + U_j\frac{\partial k}{\partial x_j} = \frac{\partial}{\partial x_j}\left[\left(\nu + \frac{\nu_t}{\delta_k}\right)\frac{\partial k}{\partial x_j}\right] + P_k - \varepsilon,$$

$$\frac{\partial \varepsilon}{\partial t} + U_j\frac{\partial \varepsilon}{\partial x_j} = \frac{\partial}{\partial x_j}\left[\left(\nu + \frac{\nu_t}{\delta_\varepsilon}\right)\frac{\partial \varepsilon}{\partial x_j}\right] + C_{1\varepsilon}\frac{\varepsilon}{k}P_k - C_{2\varepsilon}\frac{\varepsilon^2}{k} - R.$$

Here, R is an RNG-specific correction term accounting for variable turbulent dissipation. By incorporating flow deformation rates and diffusion effects, the RNG model provides superior accuracy and stability in regions with curved flows, swirl, and sharp gradients compared to the standard $k{-}\varepsilon$ approach. Alternatively, the $k{-}\omega$ model characterizes the flow using turbulent kinetic energy (k) and its specific dissipation rate (ω). While highly accurate for resolving near-wall flows, thin boundary layers, and low-Reynolds-number aerodynamics, its pronounced sensitivity to free-stream turbulence in open regions can introduce uncertainties. This limitation is precisely why it is integrated into the SST formulation (blending near-wall $k{-}\omega$ with far-field $k{-}\varepsilon$). The standard $k{-}\omega$ transport equations are expressed as:

$$\frac{\partial(\rho k)}{\partial t} + \frac{\partial(\rho U_j k)}{\partial x_j} = \frac{\partial}{\partial x_j}\left[\left(\mu + \frac{\mu_t}{\sigma_k}\right)\frac{\partial k}{\partial x_j}\right] + P_k - \beta^*\rho k\omega,$$

$$\frac{\partial(\rho\omega)}{\partial t}+\frac{\partial(\rho U_j\omega)}{\partial x_j}=\frac{\partial}{\partial x_j}\left[\left(\mu+\frac{\mu_t}{\delta_\omega}\right)\frac{\partial\omega}{\partial x_j}\right]+\alpha\frac{\omega}{k}P_k-\beta^*\rho\omega^2.$$

The Transition SST (Shear-Stress Transport) model improves upon the standard $k-\omega$ approach by blending it with the $k-\varepsilon$ formulation. It is specifically designed to accurately resolve high-velocity gradients and the complex transition regimes between laminar and turbulent flows [16]. The governing equations are defined as:

$$\frac{\partial}{\partial x_i}(\rho k u_i)=\frac{\partial}{\partial x_j}\left[(\mu+\delta_k\mu_t)\frac{\partial k}{\partial x_j}\right]+\gamma G_k-Y_k^*+S_k,$$

$$\frac{\partial}{\partial x_i}(\rho\alpha u_i)=\frac{\partial}{\partial x_j}\left[(\mu+\delta_\omega\mu_t)\frac{\partial\omega}{\partial x_j}\right]+G_\omega-Y_\omega^*+D_\omega+S_\omega.$$

Capturing the laminar-to-turbulent transition is crucial for accurately determining the lift and drag characteristics of VAWT blades. To achieve this, the Transitional SST model was implemented. By incorporating an additional transport equation for the intermittency factor (gamma), this model effectively triggers and resolves the transition process within the boundary layer. The use of this model is particularly advantageous for several key reasons. First, unlike standard RANS models that assume fully turbulent flow, the Transitional SST formulation is explicitly designed for low-Reynolds-number regimes ($\mathrm{Re} < 10^5$), perfectly aligning with the 3–5 m/s wind speeds investigated in this study. Furthermore, it accurately predicts the onset of boundary layer separation, dynamic stall, and vortex shedding by reliably resolving the transitional layers near the highly unsteady rotating blades. Finally, this model provides superior predictive accuracy. Standard models lacking transition corrections, such as the standard $k-\varepsilon$ model, often fail to capture aerodynamic "dead zones"and localized pulsations, leading to a significantly overestimated power coefficient (C_p). By contrast, the proper application of the Transitional SST formulation ensures that near-wall flows are resolved with high fidelity. This reliability is critical for the subsequent validation of numerical results against experimental data, providing a robust aerodynamic analysis of the turbine's performance in complex, non-steady flow environments.

Let us formulate the conditions for the uniqueness of the solution to the problem. following $G_1=(x^2+y^2=R^2\cap x\leqslant 0)$ input conditions were imposed:

$$u_{G1}=U_0,\ v_{G1}=0,\ w_{G1}=0,\ p_{G1}=0,\ \varepsilon_{G1}=0,\ k_{G1}=0,\ \omega_{G1}=0.$$

Symmetry conditions were imposed on the boundary: $G_2=((0\leqslant x\leqslant L_x)\cap|y|=L_y)$

$$\frac{\partial u_{G2}}{\partial y}=0,\ v_{G2}=0,\ \frac{\partial w_{G2}}{\partial y}=0.$$

At the exit from G_3 the section, $x=L_x$ the conditions of smooth conjugation were realized:

$$\frac{\partial u_{x=L_x}}{\partial y}=0,\ \frac{\partial v_{x=L_x}}{\partial y}=0,\ \frac{\partial w_{x=L_x}}{\partial y}=0.$$

The span boundaries and working surfaces constitute the set G4. On these surfaces, the spanwise velocity along the z-axis is zero, while the X and Y components are determined by the rotational speed (ωt). Pressure boundary conditions at G_4 and at the lateral boundaries are derived from the adjacent velocity field. To simulate realistic urban and suburban environments, an inlet velocity of 3–5 m/s was prescribed. An inlet turbulence

intensity of I = 3% was adopted, consistent with standard benchmarks for small-scale VAWTs in low-roughness terrains [12, 20]. This intensity level accurately reflects low-altitude atmospheric conditions and ensures stable boundary-layer transitions without triggering non-physical numerical oscillations. Furthermore, the turbulence length scale (l) was derived from the domain's hydraulic diameter to properly initialise the turbulent kinetic energy (k) and dissipation rates. For the solid interfaces (turbine blades and ground), no-slip boundary conditions were applied. The near-wall mesh was appropriately refined to maintain y+ values within the valid range for the SST and RNG models, which is essential for accurately capturing flow separation. Within COMSOL Multiphysics, a hybrid coordinate mapping was implemented, seamlessly linking polar coordinates in the rotating rotor zone with Cartesian coordinates in the stationary far-field. This approach, coupled with physically coherent turbulence initialisation, significantly enhances the fidelity of the numerical predictions, particularly in resolving the unsteady wake development downstream of the turbine.

3D CFD simulations were performed in COMSOL Multiphysics using a rotating machinery solver and parallel computing to evaluate unsteady wind-rotor interactions. A hybrid mesh was implemented: hexahedral elements in the stationary domain, tetrahedral cells around the complex blade-hinge geometry, and prismatic layers near solid boundaries to resolve the viscous sublayer. Local refinement and strict mesh quality controls were applied to minimize numerical diffusion.

The 3D VAWT geometry was generated in COMSOL Multiphysics using array and duplication features to assemble the full rotor by rotating the primary span at 90°, 180°, and 270°. The baseline frame consists of four perpendicular spans, with blades positioned between crossbars at an optimised pitch angle of 25°, which maximises starting torque and delays dynamic stall. Transient structural rotation was handled via coordinate transformations using a rotation matrix about the central axis with angular velocity ω_t. To ensure domain integrity, the computational domain was configured with a uniform velocity inlet of 4–5 m/s incorporating atmospheric turbulence parameters, a zero-gauge-pressure outlet to allow undisturbed wake development, and symmetry planes on the top and lateral boundaries to prevent blockage effects. Standard no-slip conditions were applied to all solid walls, including the blades and shaft, to accurately capture skin friction and flow separation.

Boundary conditions on the solid walls strictly enforce the standard no-slip condition [10–12], defined as:

$$u|_{l_w=0} = 0, l_w = \frac{h}{2},\ \nabla k \cdot n = 0,\ \omega = \sqrt{\omega_{\text{visc}}^2 + \omega_{\log}^2}.$$

The turbulent flow parameters at the inlet are derived from the specified turbulence intensity (I = 3%) and the hydraulic diameter (D_g):

$$k = \frac{3}{2}(IU_{\text{in}})^2,\ \varepsilon = C_\mu^{\frac{3}{4}} \frac{k^{\frac{3}{2}}}{l},\ l = 0.07D_g,\ I = 3\%.$$

The governing equations were resolved using a Fully Coupled approach with the PARDISO direct solver and a damped Newton method (damping factor of 0.1), setting a threshold of 1000 iterations per simulation. Solution convergence was monitored based on the residuals of continuity, momentum, and turbulence transport equations, with a stringent convergence criterion of 10^{-5} imposed alongside the stabilization of integral quantities like rotor torque and power coefficient (C_p). To ensure numerical reliability,

the maximum cell skewness was maintained below 0.82 with an average of 0.23. Furthermore, for accurate prediction of boundary layer detachment under the SST k-omega formulation, the first prismatic layer thickness was explicitly sized to maintain y+=1 uniformly across all turbine blades.

3 Results and discussion

This section analyzes the 3D numerical simulation results, focusing on the VAWT's aerodynamic performance, turbulent flow fields, and surface pressure distributions. The effects of key geometric and operational parameters are evaluated and validated against empirical data to establish the optimal design configuration. Simulations were conducted at discrete rotor angles (α = 0°, 15°, 30°, 45°, 60°, and 75°). Figure 3 illustrates the horizontal velocity magnitude (U) in the XY plane at the central probe location $(0, 1.25, 0)$, corresponding to the turbine's horizontal midpoint at $\alpha = 0°$. Tracking velocity at this central coordinate is essential for evaluating the primary aerodynamic parameters.

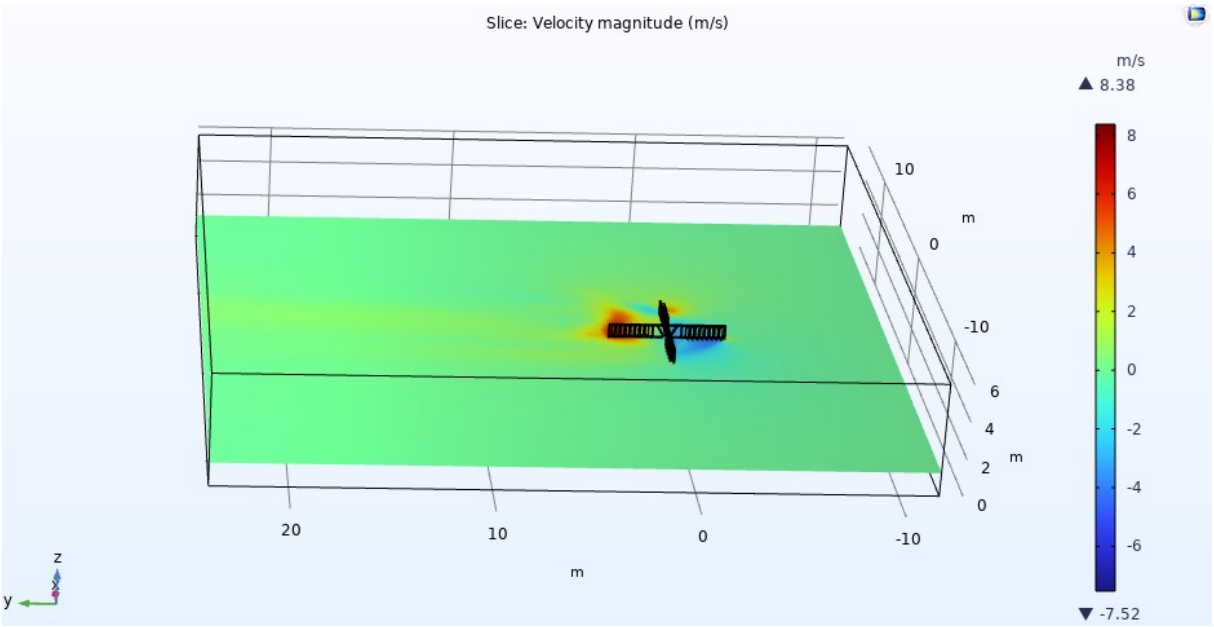

Figure 3 Field of y-components of velocities and U (m/s) (The unit should be in upright/regular font) at $z = 1.25$ m, $\alpha = 0°$

At the rotor's mid-span, the longitudinal velocity ranges from $U_{\max} = 8.38$ m/s to $U_{\min} = -7.52$ m/s, with the peak velocity attenuating toward the blade extremities. High-velocity zones predominantly develop around the two windward blades intercepting the primary airflow. Conversely, the two leeward blades induce significant aerodynamic resistance, generating localized reverse flow and distinct wake regions. Because capturing the full 3D spatial evolution of these velocity deficits, flow deflections, and wake formations is experimentally prohibitive, they were evaluated numerically to provide a deeper physical interpretation of the turbine's aerodynamic behavior, revealing dynamic flow fluctuations across varying azimuthal angles. The maximum and minimum velocities ($U_{\max}/U_{\min}$) were recorded as follows: 7.82/–8.55 m/s at $\alpha = 15°$; 6.86/–8.32 m/s at $\alpha = 30°$; 6.93/–6.66 m/s at $\alpha = 45°$; 7.89/–5.67 m/s at $\alpha = 60°$; and 8.74/–6.72 m/s at $\alpha = 75°$.

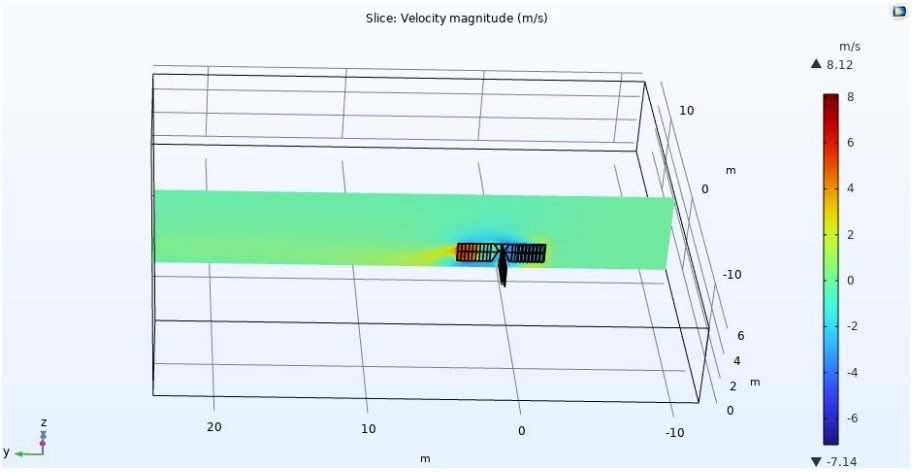

Figure 4 Change in the modulus U_y of the velocity vector component in the vertical section of the middle of the cross section at $\alpha = 0°$

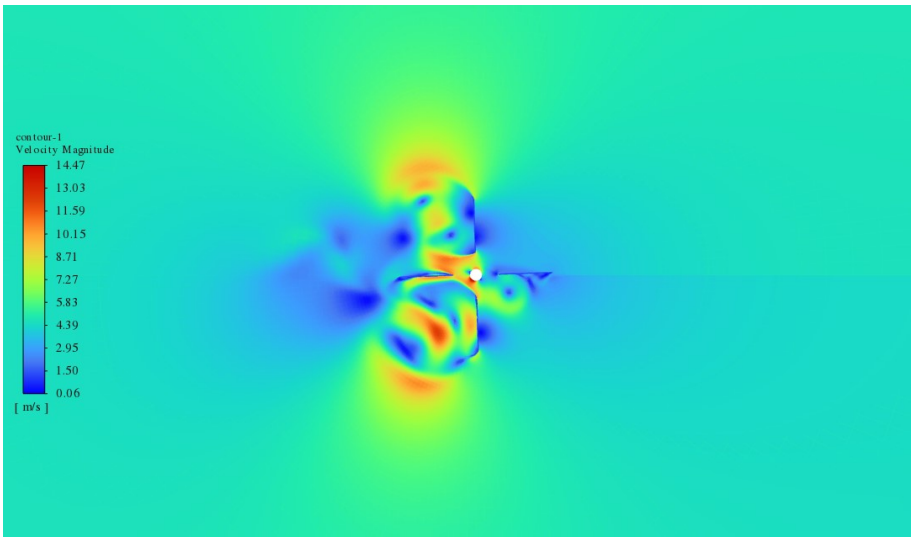

Figure 5 Rotation speed contour V=8 m/s

Fig. 4 illustrates the transverse velocity component (U_y) within the central vertical plane at $\alpha = 0°$. In the YZ plane, the maximum and minimum longitudinal velocities ($U_{\max}/U_{\min}$) vary dynamically with the azimuthal angle (α) as follows: 8.12/7.14 m/s at 0°; 6.88/5.69 m/s at 15°; 5.50/–5.43 m/s at 30°; 4.73/–4.51 m/s at 45°; 3.95/–3.20 m/s at 60°; and 4.28/–3.98 m/s at 75°. The highly negative velocities ($U_{\min}$) indicate large-scale flow separation and recirculation bubbles on the leeward side, which typically induce negative torque in conventional VAWTs due to aerodynamic drag. However, the proposed passive-pitch mechanism allows the returning blades to align with the free stream (opening up to 90°), restricting wake expansion, minimizing frontal blockage, and significantly reducing the opposing torque to maintain stable rotation at low wind speeds. The spatial evolution of the flow field is visualized across sequential transverse sections at $x = -$ -10, –3.5, 3.5, 11 and 18.5 m, where the upstream section at $x = -10$ m captures the undisturbed free-stream flow as a baseline reference.

The flow resistance and overall turbine efficiency are heavily influenced by localized aerodynamic phenomena. Setting the blade pitch angle to 25° induces a complex flow

topology; at $x = -3.5$ m, the flow decelerates and deforms due to the rotor's blockage effect, concentrating severe velocity and pressure gradients near the rotor. Moving downstream into the wake, static pressure recovers to free-stream values faster than the velocity deficits. The numerical contours in These flow reversals are driven by dynamic stall and severe boundary layer separation, occurring when the effective angle of attack exceeds the airfoil's critical stall limit and triggers flow detachment from the suction surface. This detachment manifests as large recirculation bubbles that impair performance by increasing pressure drag and generating negative torque.

Experimental investigations were conducted using a physical prototype to validate the CFD predictions under low-wind conditions. The experimental setup utilized a calibrated cup anemometer to monitor the incoming air stream velocity, and a laboratory test bench with magnetic holders to measure rotor shaft rotational speed and torque. Turbine performance was evaluated using the non-dimensional power coefficient (C_p) as a function of the tip speed ratio (TSR, lambda). To contextualize this approach, prior studies, such as the comparative analysis of a conventional HAWT and an Avanz-inspired design, have shown that a broader performance plateau on the C_p vs. TSR curve indicates superior self-starting capabilities and high adaptability to fluctuating low-wind environments. Aligned with these principles, the numerical results demonstrate that the proposed novel VAWT achieves high aerodynamic efficiency, as illustrated by the C_p vs. TSR relationship in Figure 6.

As illustrated, the maximum power coefficient peaks at $C_p = 0.35$ at an optimal tip speed ratio of TSR = 2.8, making the proposed design highly competitive with conventional industry-standard Darrieus turbines. Derived using the SST turbulence model, this correlation accurately captures the delayed flow separation achieved by the 25° blade pitch angle, which directly enhances the lift force. Notably, the turbine maintains a broad and stable operational plateau (TSR = 1.5 to 4.0), ensuring consistent efficiency under fluctuating wind conditions. The primary experimental outcome—the total power output of the wind generator at a base orientation of $\alpha = 0°$—is summarized in Table 1, providing a robust baseline for direct comparison with the simulated results.

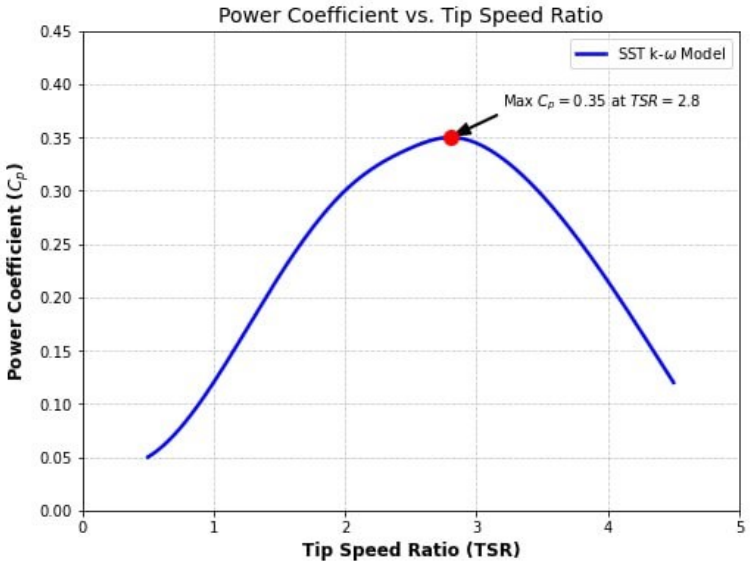

Figure 6 Variation of power coefficient (C_p) with tip speed ratio (TSR) for the proposed VAWT at 25° pitch angle.

Table 1 Power and thrust coefficients compared with experimental data

Model	With C_p
Standard $k-\varepsilon$	0.325
SST	0.347
RNG	0.326
k-ω	0.339
Experiment	0.356

Controlled laboratory experiments were conducted using a test bench comprising a controllable airflow system, a generator-coupled rotor, and data acquisition instrumentation across wind velocities of 3–8 m/s monitored by a calibrated anemometer. A tachometer and precision torque sensors continuously recorded the turbine's rotational speed, torque, and electrical power output. All tests were repeated multiple times to ensure data reliability by acquiring averaged values. Overall measurement uncertainties were rigorously evaluated using standard error propagation methods, accounting for both manufacturer-specified instrument accuracy and statistical variance. As summarized in Table 2, the experimental key performance indicators—specifically torque and the power coefficient—exhibited strong agreement with the CFD predictions. This alignment robustly confirms the validity of the computational model and the selected simulation parameters.

Table 2 Comparison of power coefficients and relative errors with experimental data

Model	Relative Error (%)
Standard $k-\varepsilon$	8.71
SST	3.37
RNG	8.43
k-ω	4.77
Experiment	0.00

Relative errors were computed by comparing the numerical predictions of each turbulence model with the experimental data. The SST model showed the best agreement, with the lowest deviation (3.37%), and was therefore selected as the primary solver. The primary justification for using the SST formulation is its exceptional ability to resolve laminar-to-turbulent transition at low Reynolds numbers. Unlike conventional models (such as standard k-epsilon, RNG, and k-omega) that assume fully turbulent flow, the Transitional SST model physically resolves the boundaries between laminar, transitional, and turbulent regimes. This ensures high-fidelity approximations of critical aerodynamic forces, shear flows, vortex shedding, and flow separation zones around the blades, providing a robust computational foundation for reliable design optimisation.

Table 3 The highest and lowest values of longitudinal velocity in the flow region are given for different values of the angle α

Corner α, degree	**0**	**15**	**30**	**45**	**60**	**75**
$U_{\max}$(m/s)	6.1	6.49	6.38	5.87	6.4	6.95
$U_{\min}$(m/s)	-0.966	-0.605	-1.42	-3.25	-5.52	-6.66

The non-monotonic behavior of these parameters is attributed to the aerodynamic braking effect of the blades and their relative spatial orientation at various azimuthal angles (α). A comparison of the maximum and minimum transverse flow velocities across different α values is summarized in Table 4.

Table 4 The greatest and least transverse flow velocity in the flow region at different angle values α

Corner α, degree	**0**	**15**	**30**	**45**	**60**	**75**
$V_{\max}$(m/s)	3.59	2.01	3.13	3.71	4.65	4.3
$V_{\min}$(m/s)	-4.12	-4.06	-4.36	-4.99	-4.2	-3.96

At low wind speeds (3 m/s), the VAWT's aerodynamic performance is governed by complex boundary-layer dynamics, particularly localised flow separation on the leeward blade surfaces. Although separation typically degrades torque and the power coefficient, the optimised blade geometry promotes rapid flow reattachment, limiting separation bubbles and sustaining aerodynamic loading. Pressure-distribution analysis reveals strong gradients across the blades that drive rotor rotation, while the velocity field shows accelerated flow near the blade tips and controlled downstream wake expansion, indicating efficient momentum extraction. Concurrently, turbulence intensity remains localised within near-wall regions, minimising parasitic energy dissipation. The synergistic interplay of controlled boundary-layer separation, favourable pressure gradients, and mitigated turbulence underpins the turbine's robust low-speed performance, validating that coupling geometric optimisation with high-fidelity turbulence modelling is critical for developing efficient VAWTs tailored for low-wind regions.

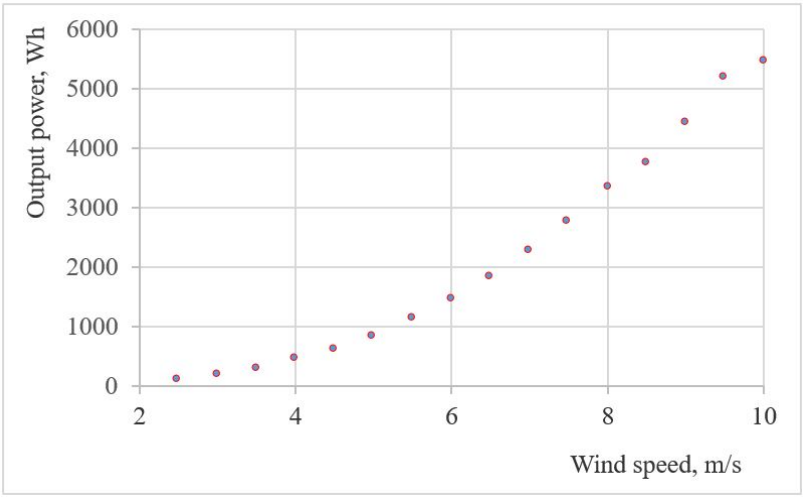

Figure 7 Wind turbine power curve

Figure 7 illustrates the electrical energy output of the optimised VAWT. The data demonstrate a significant performance advantage over conventional counterparts, primarily due to its enhanced low-wind-speed operation. By achieving a lower cut-in speed, the proposed design harvests substantially more cumulative energy than standard devices that require higher wind speeds to initiate power generation.

4 Conclusions

This study presents a comprehensive 3D numerical and experimental investigation of a novel VAWT optimised for low-wind environments. Among the evaluated RANS models, the SST formulation demonstrated the highest accuracy, effectively leveraging its hybrid blending mechanism to resolve near-wall adverse pressure gradients and dynamic flow separation, whereas the RNG model overpredicted turbulent viscosity and the standard k-omega model exhibited excessive sensitivity to the free stream. Empirical validation confirmed stable energy ex-traction at wind speeds as low as 3 m/s. This high efficiency is primarily driven by the innovative passive blade-pitch control mechanism, which significantly mitigates negative torque during the return stroke, yielding a higher net power coefficient (C_p) than conventional fixed-blade designs. Ultimately, this synergistic analysis establishes a robust framework for optimising small-scale VAWTs, providing actionable insights to advance decentralised wind energy harvesting in urban and suburban regions.

References

[1] De Tavernier K.A.M., Ferreira C., Goude A. *Vertical-axis wind turbine aerodynamics // Handbook of Wind Energy Aerodynamics Springer.* – 2022. – Vol. 1. – P. 1327–1355. doi: http://dx.doi.org/10.1007/978-3-030-05455-7_64-2.

[2] Hara Y., Moral M.S., Ide A., Jodai Y. *Fast Simulation of the Flow Field in a VAWT Wind Farm Using the Numerical Data Obtained by CFD Analysis for a Single Rotor // Energies.* – 2025. – Vol. 18. – № 1. – Art. 220. doi: http://dx.doi.org/10.3390/en18010220.

[3] Sun Zhu J., Hanif A., Li Z., Sun G. *Effects of blade shape and its corresponding moment of inertia on self-starting and power extraction performance of the novel bowl-shaped floating straight-bladed vertical axis wind turbine // Sustainable Energy Technologies and Assessments.* – 2020. – Vol. 39. – P. 100648. doi: http://dx.doi.org/10.1016/j.seta.2020.100648.

[4] Devesse K., Lanzilao L., Jamaer S., Van Lipzig N., Meyers J. *Including realistic upper atmospheres in a wind-farm gravity-wave model // Wind Energy Science.* – 2022. – Vol. 7. – № 4. – P. 1367–1382. doi: http://dx.doi.org/10.5194/wes-7-1367-2022.

[5] Meneveau C., Shen L., Yang D. *Effect of downwind swells on offshore wind energy harvesting–a large-eddy simulation study // Renewable Energy.* – 2014. – Vol. 70. – P. 11–23. doi: http://dx.doi.org/10.1016/j.renene.2014.03.069.

[6] Porté-Agel F. *A hybrid physics-based and data-driven model for intra-day and day-ahead wind power forecasting considering a drastically expanded predictor search space // Applied Energy.* – 2024. – Vol. 368. – P. 123375. doi: http://dx.doi.org/10.1016/j.apenergy.2024.123375.

[7] Blocken B., Carmeliet J., Stathopoulos T. *Pedestrian-level wind conditions around buildings: Review of wind-tunnel and CFD techniques and their accuracy for wind comfort assessment // Building and Environment.* – 2016. – Vol. 100. – P. 50–81. doi: http://dx.doi.org/10.1016/j.buildenv.2016.02.004.

[8] Liu Q.S., Miao W.P., Li C., et al. *Effects of trailing-edge movable flap on aerodynamic performance and noise characteristics of VAWT // Energy.* – 2019. – Vol. 189. – P. 116271. doi: http://dx.doi.org/10.1016/j.energy.2019.116271.

[9] Rose J., Natarajan S.G., Gopinathan V.T. *Biomimetic flow control techniques for aerospace applications: A comprehensive review* // *Reviews in Environmental Science and Bio/Technology*. – 2021. – Vol. 20. – № 3. – P. 645–677. doi: http://dx.doi.org/10.1007/s11157-021-09583-z.

[10] Zhu H., Hao W., Li C., et al. *A critical study on passive flow control techniques for straight-bladed vertical axis wind turbine* // *Energy*. – 2018. – Vol. 165. – P. 12–25. doi: http://dx.doi.org/10.1016/j.energy.2018.09.072.

[11] Huang S., Qiu H., Wang Y. *Aerodynamic performance of horizontal axis wind turbine with application of dolphin head-shape and lever movement of skeleton bionic airfoils* // *Energy Conversion and Management*. – 2022. – Vol. 267. – P. 115803. doi: http://dx.doi.org/10.1016/j.enconman.2022.115803.

[12] Jiang R., Zhao Z., Liu H., Ma Y., Wang T., et al. *Effect of vortex generator orientation on wind turbines considering the three-dimensional rotational effect* // *Ocean Engineering*. – 2023. – Vol. 267. – P. 113307. doi: http://dx.doi.org/10.1016/j.oceaneng.2022.113307.

[13] Seel F., Lutz T. *Numerical study of the unsteady blade root aerodynamics of a 2MW wind turbine equipped with vortex generators* // *Wind Energy Science*. – 2023. – Vol. 8. – № 9. – P. 1369–1396. doi: http://dx.doi.org/10.5194/wes-8-1369-2023.

[14] Zhang Z., Kuang L., Han Z., Zhou D., Zhao Y., Bao Y., et al. *Comparative analysis of bent and basic winglets on performance improvement of horizontal axis wind turbines* // *Energy*. – 2023. – Vol. 281. – P. 128252. doi: http://dx.doi.org/10.1016/j.energy.2023.128252.

[15] Damiola L., Siddiqui M.F., Runacres M.C., De Troyer T. *Influence of free-stream turbulence intensity on static and dynamic stall of a NACA 0018 aerofoil* // *Journal of Wind Engineering and Industrial Aerodynamics*. – 2023. – Vol. 232. – P. 105270. doi: http://dx.doi.org/10.1016/j.jweia.2022.105270.

[16] Li Y., Wang H., Wu Z. *Aerodynamic characteristic of wind turbine with the leading edge slat and Microtab* // *Sustainable Energy Technologies and Assessments*. – 2022. – Vol. 52. – P. 101957. doi: http://dx.doi.org/10.1016/j.seta.2022.101957.

[17] Zaki A., Abdelrahman M.A., Ayad S.S., Abdellatif O.E. *Effects of leading edge slat on the aerodynamic performance of low Reynolds number horizontal axis wind turbine* // *Energy*. – 2022. – Vol. 239. – P. 122338. doi: http://dx.doi.org/10.1016/j.energy.2021.122338.

[18] Abbas Z., Waqas M., Saleem Khan S., et al. *Numerical and experimental investigation of an Archimedes screw turbine for open channel water flow application* // *Energy Science & Engineering*. – 2024. – Vol. 12. – № 4. – P. 1350–1365. doi: http://dx.doi.org/10.1002/ese3.1649.

[19] Menter F.R. *Zonal two equation kw turbulence models for aerodynamic flows* // *23rd Fluid Dynamics, Plasmadynamics, and Lasers Conference*. – 1993. – AIAA Paper 1993-2906. doi: http://dx.doi.org/10.2514/6.1993-2906.

[20] Menter F.R., Kuntz M., Langtry R. *Ten years of industrial experience with the SST turbulence model* // *Turbulence, Heat and Mass Transfer*. – 2003. – Vol. 4. – № 1. – P. 625–632.

[21] Hamdamov M., Bozorov B., Mamataliyeva H., Ergashov D. *Numerical modeling of wind turbine with vertical axis using turbulence model k - ω in ANSYS FLUENT* // *E3S Web of Conferences*. – 2023. – Vol. 401. – Art. 02024. doi: http://dx.doi.org/10.1051/e3sconf/202340102024.

[22] Khan S., et al. *Centrifugal Compressor Stall Control by the Application of Engineered Surface Roughness on Diffuser Shroud Using Numerical Simulations // Materials.* – 2021. – Vol. 14. – № 8. – Art. 2033. doi: http://dx.doi.org/10.3390/ma14082033.

[23] Urbanowicz K., Bergant A., Stosiak M., Deptuła A., Karpenko M. *Navier-Stokes Solutions for Accelerating Pipe Flow—A Review of Analytical Models // Energies.* – 2023. – Vol. 16. – № 3. – Art. 1407. doi: http://dx.doi.org/10.3390/en16031407.

УДК 532

ВЫЧИСЛИТЕЛЬНОЕ МОДЕЛИРОВАНИЕ ВЕРТИКАЛЬНО-ОСЕВОЙ ВЕТРОЭНЕРГЕТИЧЕСКОЙ УСТАНОВКИ С ПАССИВНЫМ ИЗМЕНЕНИЕМ ШАГА ЛОПАСТЕЙ ДЛЯ УСЛОВИЙ СЛАБЫХ ВЕТРОВ

Музаффаров С.А., Маратов Х.У., Хамдамов М.М.

*sardorbekmuzaffarov50@gmail.com

Институт механики и сейсмостойкости сооружений им. М.Т. Уразбаева, 100125, Узбекистан, Ташкент, Ул. Дурмон Йули, 33.

В работе представлено трёхмерное численное исследование новой вертикально-осевой ветроэнергетической установки (ВЭУ) с уникальным аэродинамическим профилем и механизмом пассивного регулирования шага лопастей. Прямоугольные лопасти установлены на горизонтальных осях через шарнирные подшипники и свободно поворачиваются на угол до 90°, ограничиваемые системой штифтов и ремней: на рабочем ходу лопасти упираются в ограничитель для максимального улавливания энергии, а на возвратном раскрываются, снижая сопротивление, что обеспечивает эффективную работу при слабых ветрах (3–5 м/с) и устойчивый крутящий момент. После исследования сеточной независимости аэродинамика проанализирована в COMSOL Multiphysics путём решения уравнений Навье–Стокса, осреднённых по Рейнольдсу (RANS). Сопоставлены четыре модели турбулентности (SST, $k{-}\varepsilon$, $k{-}\omega$, RNG); наибольшую точность показала модель SST. Получены зависимости коэффициента мощности (C_p) от быстроходности (TSR), верифицированные по лабораторным данным (относительная погрешность $< 5\%$).

Ключевые слова: уравнения Навье–Стокса, ветротурбина, Comsol Multiphysics, вычислительная гидродинамика, возобновляемая энергия, скорость, давление.

Цитирование: *Музаффаров С.А., Маратов Х.У., Хамдамов М.М.* Вычислительное моделирование вертикально-осевой ветроэнергетической установки с пассивным изменением шага лопастей для условий слабых ветров // Проблемы вычислительной и прикладной математики. – 2026. – № 3(73). – С. 61-74.

DOI: https://doi.org/10.71310/pcam.3_73.2026.05

№ 3(73) 2026

ISSN 2181-8460

HISOBLASH VA AMALIY MATEMATIKA MUAMMOLARI

ПРОБЛЕМЫ ВЫЧИСЛИТЕЛЬНОЙ И ПРИКЛАДНОЙ МАТЕМАТИКИ

PROBLEMS OF COMPUTATIONAL AND APPLIED MATHEMATICS

AiRI
RAQAMLI TEXNOLOGIYALAR VA SUN'IY INTELLEKTNI RIVOJLANTIRISH ILMIY-TADQIQOT INSTITUTI

ПРОБЛЕМЫ ВЫЧИСЛИТЕЛЬНОЙ И ПРИКЛАДНОЙ МАТЕМАТИКИ

№ 3(73) 2026

Журнал основан в 2015 году.
Издается 6 раз в год.

Учредитель:
Научно-исследовательский институт развития цифровых технологий и искусственного интеллекта.

Журнал зарегистрирован в Агентстве информации и массовых коммуникаций при Администрации Президента Республики Узбекистан.
Свидетельство №0856 от 5 августа 2015 года.

ISSN 2181-8460, eISSN 2181-046X

Адрес редакции:
100125, г. Ташкент, м-в. Буз-2, 17А.
Тел.: +(998) 71 263-41-98.
Э-почта: journals@airi.uz.
Веб-сайт: https://journals.airi.uz.

Дизайн и вёрстка:
Шарипов Х.Д.

Отпечатано в типографии НИИ РЦТИИ.
Подписано в печать 25.06.2026 г.
Формат 60x84 1/8. Заказ №3. Тираж 100 экз.

PROBLEMS OF COMPUTATIONAL AND APPLIED MATHEMATICS

No. 3(73) 2026

The journal was established in 2015.
6 issues are published per year.

Founder:
Digital Technologies and Artificial Intelligence Development Research Institute.

The journal is registered by Agency of Information and Mass Communications under the Administration of the President of the Republic of Uzbekistan.
Certificate of Registration No. 0856 of 5 August 2015.

ISSN 2181-8460, eISSN 2181-046X

Address:
100125, Tashkent, Buz-2, 17A.
Tel.: +(998) 71 263-41-98.
E-mail: journals@airi.uz.
Web-site: https://journals.airi.uz.

Layout design:
Sharipov Kh.D.

DTAIRI printing office.
Signed for print 25.06.2026
Format 60x84 1/8. Order No. 3. Print run of 100 copies.

Содержание

Яхшибаев Д.С., Боборахимов Б.И.
Математическое моделирование поступления многофазного потока смеси в стратифицированное водохранилище и разрушения слоистой структуры . . . 7

Бахтиёров Б.Б., Хужаев И.К., Туропова Н.В.
Математическая модель и анализ гашения гидравлического удара с помощью воздушного колпака 25

Бегимов О.М., Хужаев И.К., Мамадалиев Х.А.
Исследование скорости распространения малых возмущений давления в газожидкостной среде с учетом массовой концентрации газа и деформации стенки трубопровода 37

Эргашев Д.Й., Хужаев Ж.И., Ахмаджонов С.С.
Математическая модель процесса теплоотдачи от жидкого теплоносителя, текущего по оребренному прямоугольными ребрами цилиндрическому трубопроводу 50

Музаффаров С.А., Маратов Х.У., Хамдамов М.М.
Вычислительное моделирование вертикально-осевой ветроэнергетической установки с пассивным изменением шага лопастей для условий слабых ветров 61

Хожикулов Ш.Ш., Бегимов О.М., Обиджонов А.Ж.
Исследование динамики переходных процессов, связанных с изменением расхода в конце участка трубопровода, с учетом и без учета силы сопротивления 75

Равшанов Ш.А., Боборахимова М.И., Чуллиев Ш.И.
Моделирование тепло- и массообмена в рельефном трубопроводе с постоянными и изменяющимися диаметрами 90

Равшанов Н., Боборахимов Б.И., Бердиёров Ш.Ш.
Характеристики загрязнения мембраны в процессе фильтрации и транспортировки в цилиндрическом пористом фильтре 104

Халджигитов А.А., Бобоназаров А.А., Рахмонова Р.А., Тиловов О.О.
Численное моделирование задач теории упругости в напряжениях методом конечных элементов 125

Тиловов М.А.
Численное исследование динамики производных различного порядка уравнения Фолкнера–Скэна в зависимости от градиента давления 139

Жумаев З.З.
Приближённое решение задач с начальными условиями для дифференциальных уравнений первого порядка с использованием комбинированного метода Рунге–Кутты и метода с кусочно-постоянным аргументом 153

Contents

Yakhshibaev D.S., Boborakhimov B.I.
Mathematical modeling of multiphase mixture inflow into a stratified reservoir and the breakdown of the layered structure 7

Bakhtiyorov B.B., Khujaev I.K., Turapova N.V.
Mathematical model and analysis of water hammer damping using an air vessel . 25

Begimov O.M., Khujaev I.K., Mamadaliev Kh.A.
Investigation of the propagation velocity of small pressure disturbances in a gas–liquid medium with account for gas mass concentration and pipeline wall deformation 37

Ergashev D.Y., Khujaev J.I., Akhmadjonov S.S.
A mathematical model of heat transfer from a liquid coolant flowing through a cylindrical pipeline finned with rectangular fins 50

Muzaffarov S.A., Maratov Kh.U., Hamdamov M.M.
Computational modeling of a passive-pitch low-wind vertical-axis wind turbine . 61

Khozhikulov Sh.Sh., Begimov O.M., Obidjonov A.J.
Investigation into the dynamics of transient processes associated with flow rate changes at the end of a pipeline section, both with and without resistance force . 75

Ravshanov Sh.A., Boborakhimova M.I, Chulliev Sh.I.
Modelling heat and mass transfer in a relief pipeline with constant and varying diameters 90

Ravshanov N., Boborakhimov B.I., Berdiyorov Sh.Sh.
Membrane fouling characteristics during filtration and transport processes in a cylindrical porous filter 104

Khaldjigitov A.A., Bobonazarov A.A., Rakhmonova R.A., Tilovov O.O.
Numerical modeling of elasticity theory problems in terms of stresses using the finite element method 125

Tilovov M.A.
Numerical study of the dynamics of derivatives of various orders of the Falkner–Skan equation depending on the pressure gradient 139

Jumaev Z.Z.
Approximate solution of initial value problems for first-order differential equations using a combined Runge-Kutta and piecewise constant argument method . 153